PAPER

Check for updates

Unraveling the effect of Al doping on CO adsorption at ZnO(10$\bar{1}$0)

D. C. Nguyen,[ab] Thanh Khoa Phung,[cd] Dai-Viet N. Vo, [iD][e] Tu Hai Le,[f] Dinh Quang Khieu[g] and Thong Le Minh Pham [iD] *[hi]

Understanding the effect of Al doping on CO adsorption at ZnO(10$\bar{1}$0) is crucial for designing a high-performance CO gas sensor. In this work, we investigated the adsorption properties of CO on pristine and Al-doped ZnO(10$\bar{1}$0) by performing DFT+U calculations. It is found that the doping of Al on ZnO(10$\bar{1}$0) induces the semiconductor-to-metal transition and thus enhances the conductance of the substrate. Compared to the pristine ZnO(10$\bar{1}$0), the adsorption energy of CO on the Al-doped surfaces is significantly enhanced since Al doping has the effect of strengthening the adsorption bond. The bonding analysis reveals that CO adsorbs on pristine ZnO(10$\bar{1}$0) *via* the sole σ-dative donation between the CO HOMO 5σ and the empty states of the Zn cation while π-back donation from filled states of Zn or Al cations to the CO 2π* LUMO is facilitated on the Al-doped surfaces. The π-back donation also results in the red-shift of the CO stretching frequency on the Al-doped surfaces, contrasting to the blue-shift on the pristine surface. The simulated results demonstrate that the doping of Al to a three-fold coordinated site on ZnO(10$\bar{1}$0) is highly beneficial for boosting the performance of the CO gas sensor. Our theoretical investigation provides fundamental insights into the effect of Al doping on the sensing mechanism for CO at the ZnO(10$\bar{1}$0) surface.

1. Introduction

Zinc oxide (ZnO) is an n-type semiconducting material with a wide bandgap and a large exciton binding energy which has attracted a growing interest for device applications owing to its great advantages such as earth-abundance, non-toxicity, and cost-effectiveness.[1] The adsorption of small gas molecules, such as H_2, O_2, CO, H_2S and NH_3 on ZnO surfaces is one of the most widely studied problems in surface science, not only because of its role as a model system to understand the gas–surface interaction but also due to its great technological importance. ZnO has become a frequently studied material for various

important applications which involve the adsorption of CO gas. For instance, ZnO has been used as a catalyst for chemical conversions such as CO oxidation reaction[2,3] and methanol synthesis from syngas (CO/H_2).[4–6] In particular, ZnO has found a very useful application in sensing materials for chemo-resistive CO gas sensors[7–10] taking advantage of its high electron mobility, its ease of fabrication, and excellent chemical and thermal stability. For this reason, understanding the adsorption properties of CO on ZnO surfaces is crucial for designing novel CO gas sensors with high sensitivity, especially for the ones that operate at ambient temperature.

ZnO nanomaterials have been synthesized, characterized, and tested for gas sensing applications in a variety of morphologies such as thin films, nanorods, nanowires, nanotubes, nanospheres, nanoparticles, *etc.*[11] Although the gas sensors using ZnO material have shown good sensing properties, the elevated operating temperatures is the main drawback which limits their extensive applications. Therefore, considerable effort has been devoted to enhancing the sensing response of the ZnO gas sensors at the ambient operating temperature, and the surface modification or doping with metal cations have been proved as a facile and effective approach.[12,13] Particularly, the experimental studies have demonstrated that the sensing response to CO of the gas sensors using ZnO nanoparticles could be enhanced by doping with Al metal.[14,15] The density functional theory (DFT) studies on ZnO nanocluster[16] and ZnO nanowire[17] have also confirmed the enhancement of CO

[a]*Laboratory of Theoretical and Computational Biophysics, Ton Duc Thang University, Ho Chi Minh City, Vietnam*

[b]*Faculty of Applied Sciences, Ton Duc Thang University, Ho Chi Minh City, Vietnam*

[c]*Department of Chemical Engineering, School of Biotechnology, International University, Ho Chi Minh City, Vietnam*

[d]*Vietnam National University, Ho Chi Minh City, Vietnam*

[e]*Center of Excellence for Green Energy and Environmental Nanomaterials (CE@GrEEN), Nguyen Tat Thanh University, 300A Nguyen Tat Thanh, District 4, Ho Chi Minh City 755414, Vietnam*

[f]*Department of Chemistry, The University of Da Nang-University of Science and Education, Da Nang City, Vietnam*

[g]*University of Sciences, Hue University, 530000, Vietnam*

[h]*Institute of Research and Development, Duy Tan University, Da Nang City 550000, Vietnam. E-mail: phamlminhthong@duytan.edu.vn*

[i]*Faculty of Environmental and Chemical Engineering, Duy Tan University, Da Nang, 550000, Vietnam*

adsorption by the effect of Al doping. In this study, we performed the first-principle calculations to understand the scientific background for the enhancement of the CO sensing response on the Al-doped ZnO sensors. We employed the periodic slab model to unravel the effect of Al doping to the adsorption properties of CO at the surfaces of ZnO nanoparticles which is more appropriate than the cluster model using in the prior study.[16] In addition, we focused on analyzing the change in the nature of bonding between CO and ZnO surface induced by the doping of Al. It is widely known that ZnO nanocrystals exhibit four dominating low Miller-index surfaces and the non-polar $ZnO(10\bar{1}0)$ has been the focus of numerous experimental and theoretical studies owing to its stable nature.[18–20] Our theoretical results indicate that Al doping not only enhances the electrical conductivity of $ZnO(10\bar{1}0)$ but also strengthens the CO adsorption. Moreover, the strengthening of the bonding of CO with Al-doped $ZnO(10\bar{1}0)$ was also clarified by analyzing the density of states (DOS), the charge density difference (CCD), and the effective Bader charge.

2. Computational methodology

The first-principles DFT[21] calculations were carried out with spin-polarization making use of the Vienna *Ab initio* Simulation Package (VASP 5.4.1).[22–25] In the VASP calculations, the interactions between ions and electrons were described by the projector augmented wave method.[26,27] The generalized gradient approximation (GGA)[28,29] with the PBE exchange–correlation functional[30] was used in this study with a cut-off energy of 450 eV for the plane-wave. A gamma-center k-point[31] with a grid size of $10 \times 6 \times 1$ was used to sample the Brillouin zone. It is widely known that plain DFT exchange–correlation functional is not adequate to describe the electronic structure of ZnO material owing to the self-interaction error.[32] Therefore, we employed the DFT+U method for the calculations in this study and the Hubbard correction U is applied only for Zn and O atoms on $ZnO(10\bar{1}0)$ surface. The chosen values of the Hubbard correction U were 10 eV and 7 eV for Zn and O respectively, which has been proven accurate in describing the position of Zn-3d and O-2p bands as well as the band gap of bulk wurtzite ZnO.[33]

The optimized bulk lattice parameters of wurtzite ZnO are $a = 3.092$ Å and $c = 4.980$ Å by the DFT+U calculation, showing good agreement with the prior theoretical result[33] using the same calculation method and the experimental value ($a = 3.242$ Å, $c = 5.188$ Å).[34] The optimized ZnO unit cell was then used to construct $ZnO(10\bar{1}0)$ which was modelled as a periodic slab consisted of 32 Zn and 32 O atoms distributed over 8 atomic layers. We considered two positions of Al dopant on $ZnO(10\bar{1}0)$, one is three-fold coordinated Zn_{3c} on the topmost layer and the other is four-fold coordinated Zn_{4c} on the second layer. The two positions of Al dopant correspond to two Al-doped surfaces, namely Al_{3c}-doped $ZnO(10\bar{1}0)$ and Al_{4c}-doped $ZnO(10\bar{1}0)$. A vertical vacuum space of 15 Å was included in the slab model to alleviate the interactions between the repeated slabs. In the course of geometry optimization, the atoms on the top 4 layers were allowed to relax to their equilibrium positions while the atoms in the bottom 4 layers were kept fixed to mimic the bulk

behaviour. The geometry optimization of adsorbed CO on the surface was considered to be convergent when the tolerance of the electronic energy (10^{-6} eV) was reached and the residue forces on each atom were less than 0.03 eV Å^{-1}. The adsorption energy (E_{ads}) of CO on the surface was defined as:

$$E_{ads} = (E_{surface} + E_{CO}) - E_{surface/CO} \qquad (1)$$

where $E_{surface}$, E_{CO} and $E_{surface/CO}$ were the total energy of the clean surface, the isolated CO molecule, and the adsorbed CO on the surface as a whole, respectively. The prior studies[35–37] have shown the importance of the dispersion correction on the adsorption of small molecules, therefore, we also calculated the adsorption energy of CO using the dispersion-corrected DFT-D3 method.[38,39]

3. Results and discussion

3.1. Effect of Al doping on the electronic structure of $ZnO(10\bar{1}0)$

It is essential to characterize the typical properties of pristine and Al-doped $ZnO(10\bar{1}0)$ before investigating the adsorption of CO. The intrinsic properties of $ZnO(10\bar{1}0)$ have been discussed in several experimental[40,41] and theoretical[42–45] studies. Therefore, we will be focussing on the effect of Al doping on the geometry and electronic properties of $ZnO(10\bar{1}0)$. The relaxed structure of $ZnO(10\bar{1}0)$ is depicted in Fig. 1a. It should be noted that Zn_{3c} and O_{3c} on the topmost layer of the slab are under-coordinated atoms with three-fold coordination. By contrast, Zn_{4c} and O_{4c} on the second layer are coordinatively saturated atoms with four-fold coordination. The coordinative unsaturation of Zn_{3c} and O_{3c} leads to a pronounced surface reconstruction on the topmost layer. In particular, the surface reconstruction of the topmost layer is indicated by the substantial contraction of Zn_{3c}–O_{3c} bond length (from 1.892 Å to 1.741 Å) and the buckling of Zn_{3c}–O_{3c} bond (buckling angle of 7.679°). The second layer also undergoes surface reconstruction although it is quite negligible. Moreover, the surface reconstruction leads to the marked difference between the bond length of the interlayer Zn_{3c}–O_{4c} bond and the intralayer Zn_{3c}–O_{3c} bond (1.815 Å *vs.* 1.741 Å). The Bader charges of Zn and O atoms displayed in Fig. 1a reveals the ionic nature of Zn–O bond where Zn is an electron donor and O is an electron acceptor. The band gap of $ZnO(10\bar{1}0)$ by our DFT+U calculation is 1.932 eV which is closer to the experimental value (3.370 eV) than the prior results (1.020 eV and 1.160 eV)[46,47] by DFT+U calculations using the same DFT package but only applying the Hubbard correction for Zn.

The calculated total energies show that Al_{4c}-doped $ZnO(10\bar{1}0)$ is thermodynamically more stable than Al_{3c}-doped $ZnO(10\bar{1}0)$ by 1.090 eV. Therefore, the substitutional doping of Al to Zn_{4c} is energetically more favourable than to Zn_{3c}. In other words, Al dopant prefers to stay at a bulk-like position than a surface-like one which is consistent with the finding from the prior DFT investigations.[46,48] The relaxed structures of the Al-doped surfaces are depicted in Fig. 1b and c. The doping of Al causes slight alterations in the surface geometry, and the most
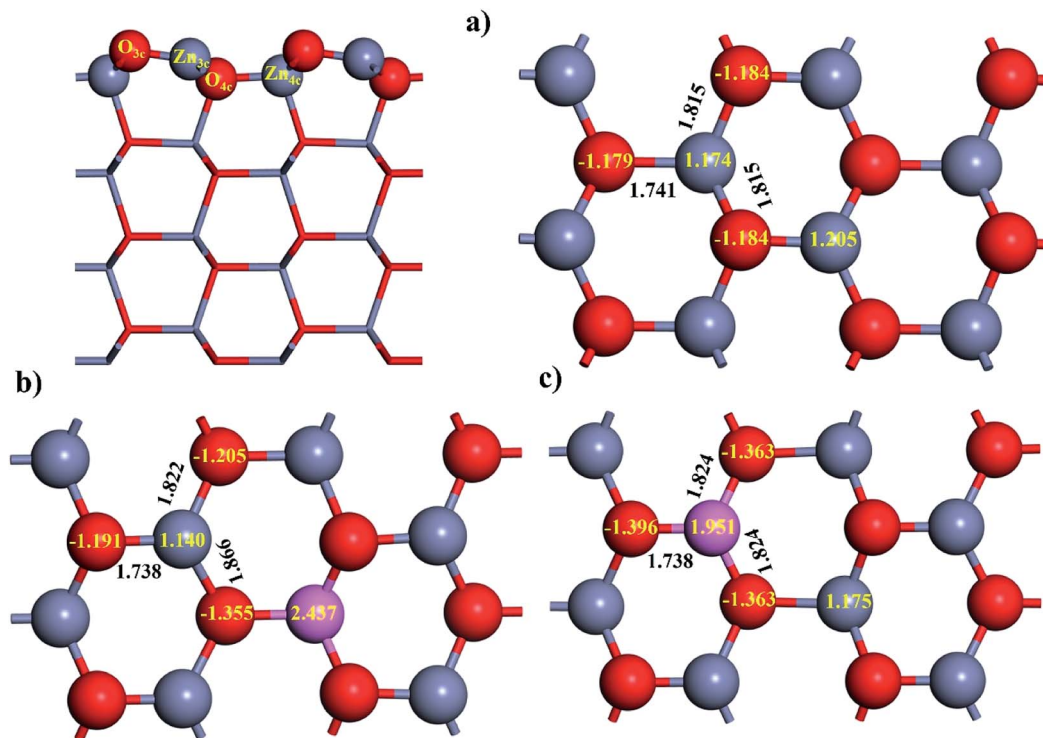
Fig. 1   Relaxed structure of: (a) ZnO($10\bar{1}0$), (b) Al$_{4c}$-doped ZnO($10\bar{1}0$), (c) Al$_{3c}$-doped ZnO($10\bar{1}0$). The insert numbers in black and yellow colors are the values for the bond length and the effective Bader charge.

noticeable changes are the bond lengths around the doping positions. For instance, Al$_{3c}$–O$_{3c}$ bonds of Al$_{3c}$-doped ZnO($10\bar{1}0$) and Zn$_{3c}$–O$_{3c}$ bonds of Al$_{4c}$-doped ZnO($10\bar{1}0$) are shorter than the corresponding bonds of the pristine surface. The total DOSs of the studied surfaces in Fig. 2a exhibit non-magnetic properties of the studied surface. Moreover, the doping of Al to ZnO($10\bar{1}0$) induces the semiconductor-to-metal transition, thus enhances the electrical conductivity of the substrate. The metallic property of Al-doped surfaces is demonstrated by the bands crossing the Fermi levels. We also calculated the Bader charge of each atom on the surfaces, and the results for Al$_{3c}$ and Al$_{4c}$ are 1.951e and 2.437e respectively. Therefore, the valence electrons residing on Al$_{3c}$ and Al$_{4c}$ are 1.049e and 0.563e respectively. These valence electrons occupy the originally empty states in the band gap of ZnO($10\bar{1}0$) and thus causing the metallic property of the Al-doped surfaces. Besides, the doping of Al results in the upward shift of the Fermi level into the conduction band as the Fermi energy of ZnO($10\bar{1}0$), Al$_{3c}$-doped ZnO($10\bar{1}0$), and Al$_{4c}$-doped ZnO($10\bar{1}0$) are −2.513 eV, −0.312 eV, and 0.187 eV respectively. The enhancement of the electrical conductivity of ZnO($10\bar{1}0$) by Al doping is consistent with the experiment result.[14] The projected DOS in Fig. 2b shows a number of Al$_{3c}$ states in the vicinity of the Fermi level, therefore, it is likely that the electrical conductivity of Al$_{3c}$-doped ZnO($10\bar{1}0$) is better than Al$_{4c}$-doped ZnO($10\bar{1}0$). Ultimately, Al doping is an effective method for tuning the conductance of ZnO($10\bar{1}0$) and the effect of Al doping on the electronic structure of ZnO($10\bar{1}0$) is similar to that of graphene-like ZnO monolayer.[49]

3.2.   CO adsorption on ZnO($10\bar{1}0$)

The adsorption properties of CO on the pristine ZnO($10\bar{1}0$) will be presented serving as the reference point for assessing the effect of Al doping on CO adsorption. The topmost layer of ZnO($10\bar{1}0$) exposes pairs of coordinately unsaturated Zn$_{3c}$ and O$_{3c}$ acting as the active sites for the adsorption of CO. Experimental studies by ultraviolet photoelectron spectroscopy found that CO adsorbs on ZnO($10\bar{1}0$) *via* the bonding between C and Zn$_{3c}$ cation.[50,51] The adsorption of CO on ZnO($10\bar{1}0$) through Zn$_{3c}$–C bond was also later confirmed by the theoretical investigations.[52,53] We also performed the geometry optimization for different orientations of CO towards ZnO($10\bar{1}0$) and found that the adsorptive structure with downward C bound to the top of Zn$_{3c}$ is the most stable one. The relaxed structure of CO adsorbed on ZnO($10\bar{1}0$) is illustrated in Fig. 3a and the adsorption properties are summarized in Table 1. As shown in Fig. 3a, CO adsorbs on ZnO($10\bar{1}0$) in a tilted geometry, and the molecular axis of CO makes with the surface normal an angle of 33.239°. It should be stressed that the tilted angle found by our DFT calculations agrees very well with the experimental value (30°).[51] We also calculated the C–O bond length and CO stretching frequency of free and adsorbed CO in order to assess their changes by the adsorption. The calculated results show that the C–O bond length is slightly reduced by 0.003 Å and the CO stretching frequency is blue-shifted by 29 cm^{-1} by the adsorption on ZnO($10\bar{1}0$) which agrees well with the experimental result[54] (26 cm^{-1}). It should be stressed that the blue-shift of CO stretching frequency also occur on the surface of other transition metal oxides such as TiO$_2$ (ref. 37 and 55) and CeO$_2$.[55] The adsorption of
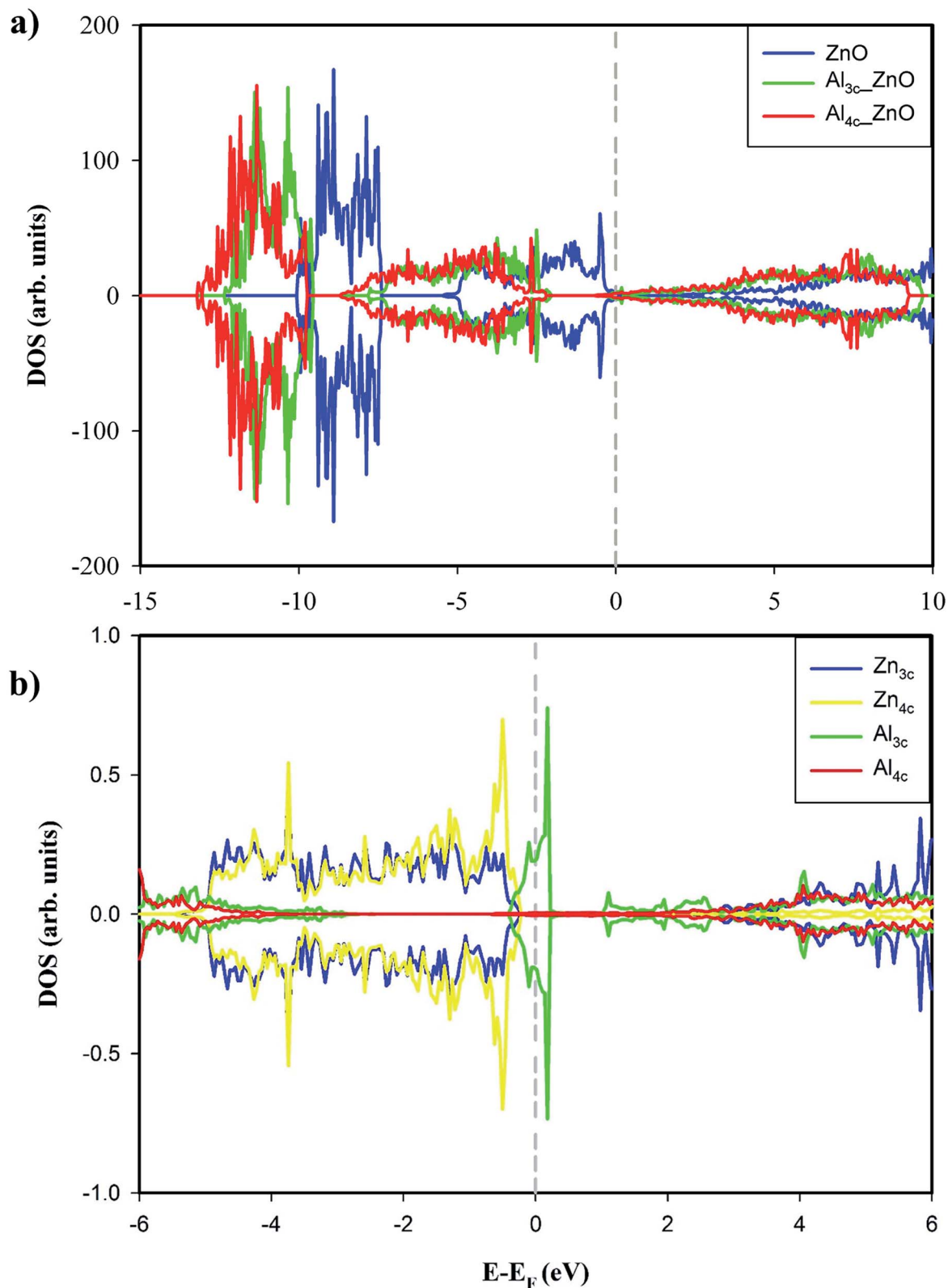
Fig. 2 (a) Total DOS of ZnO(10$\bar{1}$0), Al$_{4c}$-doped ZnO(10$\bar{1}$0) and Al$_{3c}$-doped ZnO(10$\bar{1}$0). (b) Projected DOS of Zn$_{3c}$, Zn$_{4c}$, Al$_{3c}$ and Al$_{4c}$. The Fermi levels (E_F) were shifted to 0 eV and indicated by the gray dashed lines.

CO with C-down configuration on ZnO(10$\bar{1}$0) is characterized by the adsorption energy of 0.378 eV. The CO adsorption becomes more stable when the dispersion correction was included in the

DFT calculations, and the adsorption energy reported by the DFT-D3+U calculations is 0.575 eV. The adsorption energy of CO on ZnO(10$\bar{1}$0) by our calculations is consistent with the experimental
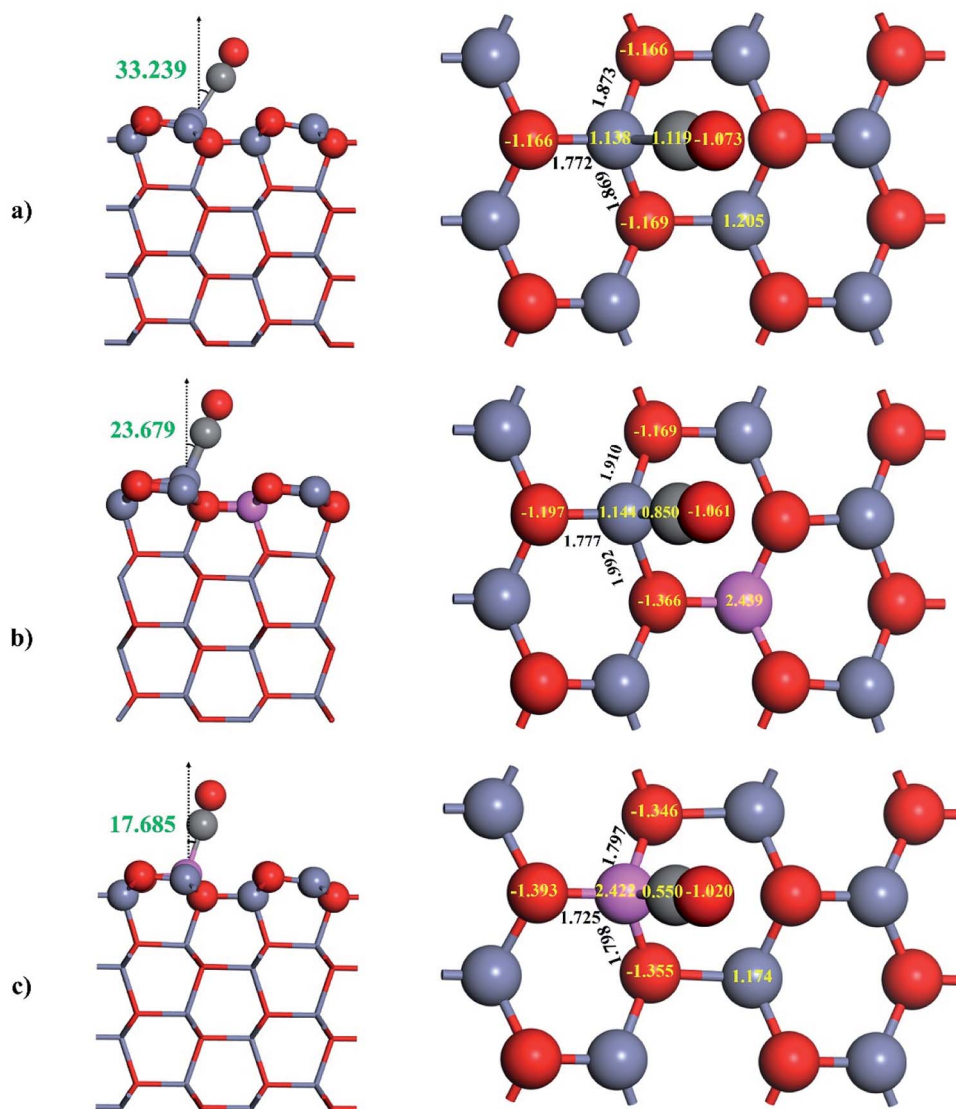
Fig. 3 Relaxed structure of adsorbed CO on: (a) ZnO(10$\bar{1}$0), (b) Al$_{4c}$-doped ZnO(10$\bar{1}$0), (c) Al$_{3c}$-doped ZnO(10$\bar{1}$0). The insert numbers in black, green and yellow colors are the values for the selected bond length, the bond angle and the effective Bader charge respectively.

value (about 0.52 eV)[51,56] and the prior theoretical results.[53,57–60] It is worth mentioning that the interaction of CO with the pristine ZnO(10$\bar{1}$0) is weak, and the adsorption is essentially physisorption.

The adsorption of CO on ZnO(10$\bar{1}$0) makes the Zn$_{3c}$–O$_{3c}$ bond become less buckled since the Zn$_{3c}$ is pulled outwardly by the interaction with CO. The outward movement of Zn$_{3c}$, in turn, causes a slight elongation of the Zn$_{3c}$–O bonds, thus

Table 1 Adsorption properties of CO on the pristine and Al-doped ZnO(10$\bar{1}$0): the adsorption energy (E_{ads}), the binding distance (d(Zn(Al)–C)), the C–O bond length (d(C–O)), the CO stretching vibrational frequency (ν(C–O)), shift of the CO stretching vibrational frequency ($\Delta\nu$(C–O)) with respect to that of free CO, and charge on adsorbed CO (Q_{CO}). The calculated C–O bond length and CO stretching vibrational frequency of free CO are 1.144 Å and 2124 cm^{-1}, respectively

Surface	Adsorption site	DFT method	E_{ads} (eV)	d(Zn(Al)–C) (Å)	d(C–O) (Å)	ν(C–O) (cm^{-1})	$\Delta\nu$(C–O) (cm^{-1})	Q_{CO} (e)
ZnO	Top of Zn	DFT+U	0.378	2.127	1.141	2153	+29	+0.046
		DFT-D3+U	0.575	2.124	1.141	—	—	—
Al$_{4c}$-doped ZnO	Top of Zn	DFT+U	0.482	1.988	1.163	1977	−147	−0.147
		DFT-D3+U	0.711	1.985	1.163	—	—	—
Al$_{3c}$-doped ZnO	Top of Al	DFT+U	1.118	1.998	1.171	1964	−160	−0.470
		DFT-D3+U	1.271	1.989	1.173	—	—	—

results in a small change in the surface geometry around the adsorption site Zn$_{3c}$. To understand the effect of CO adsorption on the electronic structure, we compared total DOSs of clean and CO-adsorbed ZnO($10\bar{1}0$) in Fig. 4a. It could be noticed that CO adsorption has a small influence on the electronic structure of the surface, and the appearance of new electronic states at
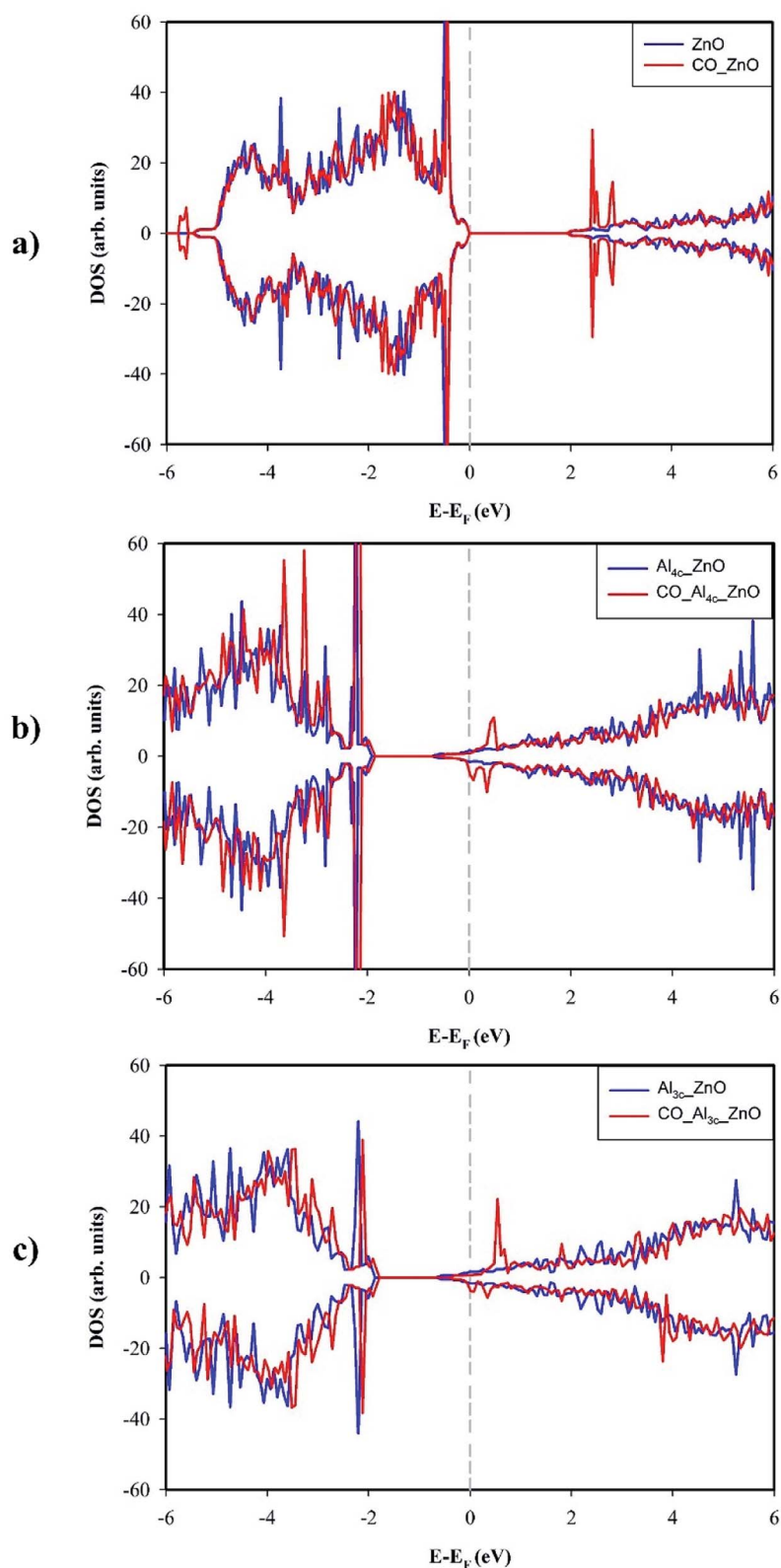

Fig. 4 Total DOS of the surface before and after CO adsorption: (a) ZnO($10\bar{1}0$), (b) Al$_{4c}$-doped ZnO($10\bar{1}0$), (c) Al$_{3c}$-doped ZnO($10\bar{1}0$). The Fermi levels (E_F) were shifted to 0 eV and indicated by the gray dashed lines.

around −5.6 eV in the valence band is the most notable feature although the intensity of these states is tiny. Moreover, the band gap of ZnO(10$\bar{1}$0) is enlarged by 0.011 eV by the adsorption of CO which results in a slight decrease in the electrical conductivity. The Bader charge analysis indicates that CO acts as an electron donor and transfers 0.046e to ZnO(10$\bar{1}$0) in the adsorption. The electronic structure and the capability towards CO adsorption explain why high-performance CO gas sensor is difficult to achieve on the pristine ZnO(10$\bar{1}$0). It is also the reason why a great research effort has been put into improving the sensing performance of ZnO material by doping with metal elements such as Al.

3.3.   CO adsorption on Al-doped ZnO(10$\bar{1}$0)

Herein, the adsorption properties of CO on Al-doped surfaces will be discussed. Fig. 3b displays the relaxed structure of CO adsorbed on Al$_{4c}$-doped ZnO(10$\bar{1}$0). The replacement of Zn$_{4c}$ by Al does not alter the way CO interacts with the surface, and CO remains adsorbed on top of Zn$_{3c}$ in the C-down configuration. However, there are some changes in the adsorptive structure, and

the most important is the decrease of Zn$_{3c}$–C bond from 2.127 Å to 1.988 Å, indicating stronger adsorption of CO on Al$_{4c}$-doped ZnO(10$\bar{1}$0) compared to the undoped surface. In fact, the adsorption energy of CO is increased by 0.104 eV (0.136 eV by DFT-D3+U) when Zn$_{4c}$ is replaced by Al dopant. By contrast to the adsorption on ZnO(10$\bar{1}$0), the C–O bond length undergoes an elongation by 0.019 Å on Al$_{4c}$-doped ZnO(10$\bar{1}$0) which results in a red-shift of CO stretching frequency by 147 cm^{-1}.

On Al$_{3c}$-doped ZnO(10$\bar{1}$0), Al$_{3c}$ cation replaces the role of Zn$_{3c}$ cation as the most adhesive site for CO, and the length of the adsorption bond Al$_{3c}$–C was found to be 1.998 Å. The tilted angle displayed in Fig. 3c (17.685°) demonstrates that adsorbed CO on Al$_{3c}$-doped ZnO(10$\bar{1}$0) is in the least inclined geometry among the adsorptive structures. The C–O bond length on Al$_{3c}$-doped ZnO(10$\bar{1}$0) is significantly elongated to 1.171 Å and the CO stretching frequency is red-shifted by 160 cm^{-1}. Consequently, the adsorption energy of CO on Al$_{3c}$-doped ZnO(10$\bar{1}$0) was found to be 1.118 eV (1.271 eV by DFT-D3+U) and is the largest adsorption energy on the studied surfaces.

Fig. 4b and c show the total DOSs of Al$_{4c}$-doped ZnO(10$\bar{1}$0) and Al$_{3c}$-doped ZnO(10$\bar{1}$0) before and after CO adsorption.
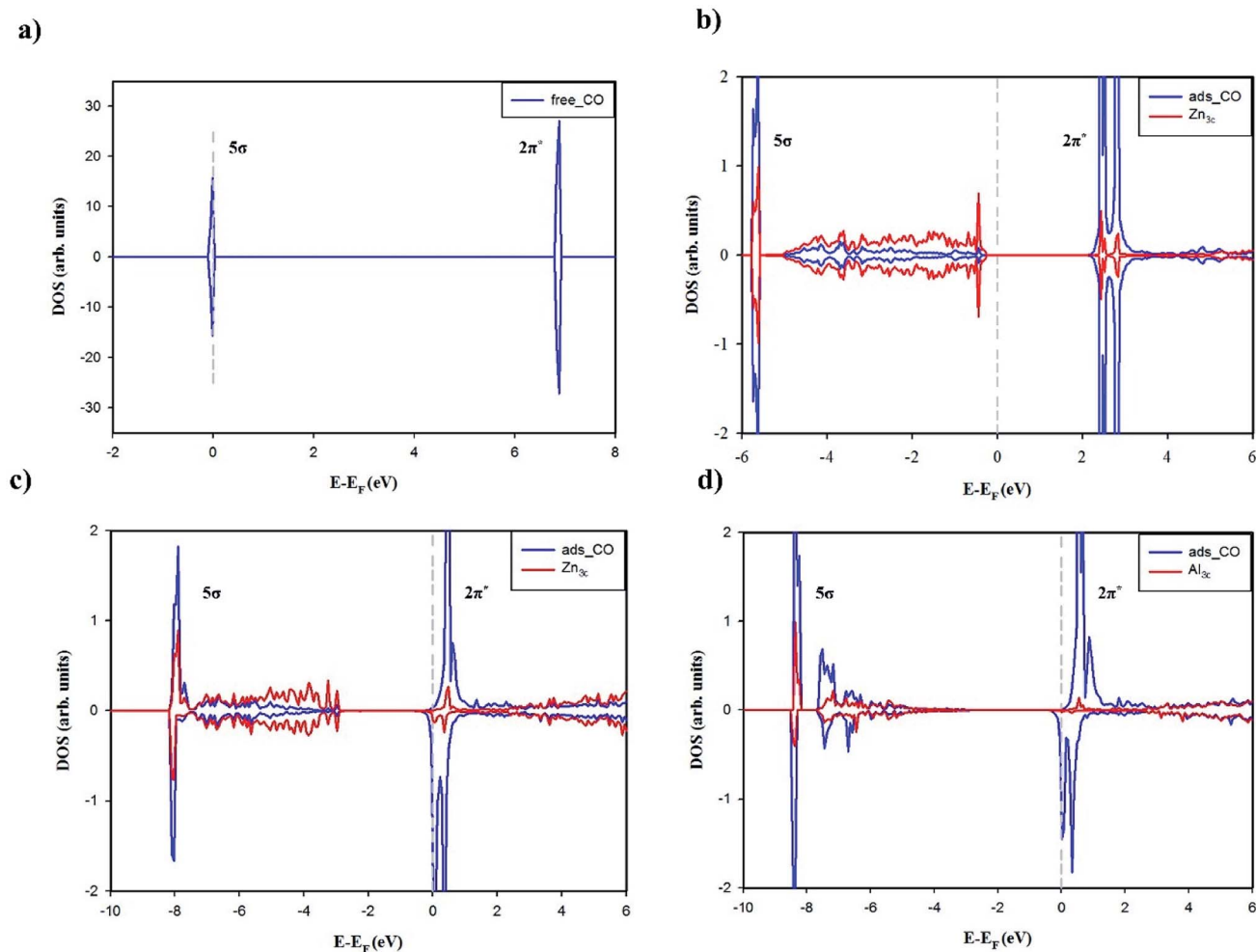

Fig. 5   Projected DOS for: (a) free CO, (b) adsorbed CO on ZnO(10$\bar{1}$0), (c) adsorbed CO on Al$_{4c}$-doped ZnO(10$\bar{1}$0), (d) adsorbed CO on Al$_{3c}$-doped ZnO(10$\bar{1}$0). The Fermi levels (E_F) were shifted to 0 eV and indicated by the gray dashed lines.

Overall, the vicinity of the Fermi level experiences slight changes caused by CO adsorption, particularly the appearance of the partially filled electronic states contributed from adsorbed CO. By contrast to the pristine surface, Al-doped counterparts are electron donors in the adsorption of CO. In particular, the Bader charge analysis reveals that Al_{4c}-doped $ZnO(10\bar{1}0)$ and Al_{3c}-doped $ZnO(10\bar{1}0)$ transfer $0.147e$ and $0.470e$ to CO respectively. It is worth noting that the electron transfer to CO from Al_{3c}-doped $ZnO(10\bar{1}0)$ is mainly from Al_{3c} cation while that from Al_{4c}-doped $ZnO(10\bar{1}0)$ is originated from the surface ions near the adsorption site Zn_{3c}.

3.4. Discussion

As have been discussed above, the adsorptions of CO on $ZnO(10\bar{1}0)$ and Al-doped $ZnO(10\bar{1}0)$ occur *via* the bonding with Zn_{3c} or Al_{3c} cation. The striking contrast in the adsorption properties is CO stretching frequency which is blue-shifted on the undoped surface but is red-shifted on the Al-doped counterparts. The adsorption of CO on $ZnO(10\bar{1}0)$ is occurred by chemical interactions, however, it has been suggested that the blue-shift of CO stretching frequency is attributed to the electrostatic interaction of CO with the electric field induced by the surface ions (the Stark effect) which results in a polarization of CO molecule.[54,61,62] The projected DOSs of free and adsorbed CO were plotted in Fig. 5 to shed light on the nature of chemical interactions between CO and the surfaces. Fig. 5a clearly demonstrates that non-bonding 5σ is the highest occupied molecular orbital (HOMO) and anti-bonding $2\pi^*$ is the lowest unoccupied molecular orbital (LUMO). Fig. 5b shows small hybridizations between the projected DOSs of CO HOMO 5σ and Zn_{3c} and the downward shift of CO HOMO 5σ after the adsorption on $ZnO(10\bar{1}0)$. Moreover, the Bader charge analysis has shown that CO donates $0.046e$ to $ZnO(10\bar{1}0)$ in the adsorption. These characteristics in combination reveal the σ-dative bond between CO HOMO 5σ and the empty states of

Zn_{3c}. Besides, the degeneracy of CO LUMO $2\pi^*$ is lifted after the adsorption which is most likely due to the polarization of CO molecule on $ZnO(10\bar{1}0)$. It is worth mentioning that the energy level of CO LUMO $2\pi^*$ is considerably higher than the Fermi energy of $ZnO(10\bar{1}0)$, thus the π-back donation from the undoped surface to CO $2\pi^*$ LUMO is not likely to occur and the adsorption bond is solely the σ-dative bond. The CDD analysis for CO adsorbed on $ZnO(10\bar{1}0)$ in Fig. 6a further validates the point. As shown in the two-dimensional CDD contour plot, the shape of the accumulation region between CO and $ZnO(10\bar{1}0)$ exhibits the characteristics of the σ-dative bond.

The adsorption energy of CO on the Al-doped surfaces is significantly larger than on the undoped counterpart, therefore it is obvious that Al doping has a profound effect on the nature of the adsorption bonds. The degree of the downward shifts of CO HOMO 5σ in Fig. 5b–d reveal the relative strength of the σ-dative bond between CO and the surfaces: $ZnO(10\bar{1}0)$ < Al_{4c}-doped $ZnO(10\bar{1}0)$ < Al_{3c}-doped $ZnO(10\bar{1}0)$. It is also worth recalling here the fact that the Fermi energy of the Al-doped surfaces is tuned upwards into the conduction band, making it closer to the energy level of CO LUMO $2\pi^*$. Thus, the π-back donations from the Al-doped surfaces to CO $2\pi^*$ LUMO are facilitated, leading to the elongation of C–O bond length and the red-shift of CO stretching frequencies. The π-back donations are also demonstrated by the partial occupations of CO LUMO $2\pi^*$ and the splitting of the projected DOSs after the adsorptions as shown in Fig. 5c and d. Moreover, the two-dimensional CDD contour plots in Fig. 6b and c also exhibit the characteristics of the π-back donations from the Al-doped surfaces to CO. The amount of charge transfer from the Al-doped surfaces to CO in the adsorption indicates that the π-back donation to CO from Al_{3c}-doped $ZnO(10\bar{1}0)$ is notably stronger than from Al_{4c}-doped $ZnO(10\bar{1}0)$ owing to a larger number of valence electrons residing on Al_{3c} than on Zn_{3c}. The relative strength of the π-back donations also demonstrates why
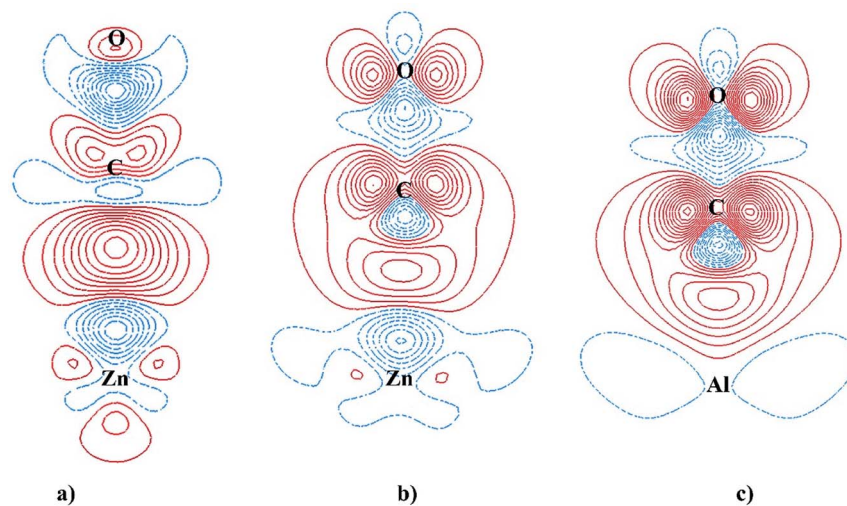

Fig. 6 Two-dimensional charge density difference contour plot for: (a) adsorbed CO on $ZnO(10\bar{1}0)$, (b) adsorbed CO on Al_{4c}-doped $ZnO(10\bar{1}0)$, (c) adsorbed CO on Al_{3c}-doped $ZnO(10\bar{1}0)$. The solid red line and dashed blue line represent an electron accumulation and an electron depletion respectively.

C–O bond length on Al_{3c}-doped $ZnO(10\bar{1}0)$ is longer than on Al_{4c}-doped $ZnO(10\bar{1}0)$. Moreover, the π-back donation dominates the σ-dative bond in the adsorption of CO on Al_{3c}-doped $ZnO(10\bar{1}0)$, making the big difference in the adsorption energy of CO on Al_{3c}-doped $ZnO(10\bar{1}0)$ and $ZnO(10\bar{1}0)$. It is interesting to note that the enhancement of CO adsorption by the effect of Al doping is also found for ZnO nanoclusters,[16] ZnO nanowire[17] and graphene-like ZnO monolayer.[49]

4. Conclusions

By performing the DFT+U calculations, we have investigated the adsorption properties of CO on pristine and Al-doped $ZnO(10\bar{1}0)$ in an effort to understand the effect of Al doping on the sensing mechanism of CO at $ZnO(10\bar{1}0)$. Two Al-doped surfaces corresponding to two doping positions of Al, three-fold coordinated site on the topmost layer and four-fold coordinated site on the second layer, were considered in this study. The electronic structure analysis reveals the metallic property of the Al-doped surfaces and thus the doping of Al to $ZnO(10\bar{1}0)$ enhances the electrical conductivity of the substrate. The adsorption of CO is stabilized on the Al-doped surfaces since Al doping has the effect of strengthening the adsorption bond. The adsorption of CO on the pristine surface is driven by the sole σ-dative bond between CO HOMO 5σ and the empty states of Zn cation while the π-back donation from the surface cation to CO 2π* LUMO is facilitated by the effect of Al doping. The π-back donation is also responsible for the red-shift of CO stretching frequency on the Al-doped surfaces. Our simulated DFT results indicate that the Al dopant at the three-fold coordinated site produces more beneficial effects on the performance of the CO gas sensor than at the four-fold coordinated site.

Conflicts of interest

The authors declare that there are no conflicts of interest regarding the publication of this paper.

Acknowledgements

References

1 Ü. Özgür, Y. I. Alivov, C. Liu, A. Teke, M. A. Reshchikov, S. Doğan, V. Avrutin, S.-J. Cho and H. Morkoç, *J. Appl. Phys.*, 2005, **98**, 041301.

2 Y. Martynova, B. H. Liu, M. E. McBriarty, I. M. N. Groot, M. J. Bedzyk, S. Shaikhutdinov and H. J. Freund, *J. Catal.*, 2013, **301**, 227–232.

3 R. G. S. Pala, W. Tang, M. M. Sushchikh, J.-N. Park, A. J. Forman, G. Wu, A. Kleiman-Shwarsctein, J. Zhang, E. W. McFarland and H. Metiu, *J. Catal.*, 2009, **266**, 50–58.

4 M. Bowker, H. Houghton and K. C. Waugh, *J. Chem. Soc., Faraday Trans. 1*, 1981, **77**, 3023–3036.

5 M. Kurtz, J. Strunk, O. Hinrichsen, M. Muhler, K. Fink, B. Meyer and C. Wöll, *Angew. Chem., Int. Ed.*, 2005, **44**, 2790–2794.

6 J. Strunk, K. Kähler, X. Xia and M. Muhler, *Surf. Sci.*, 2009, **603**, 1776–1783.

7 H.-W. Ryu, B.-S. Park, S. A. Akbar, W.-S. Lee, K.-J. Hong, Y.-J. Seo, D.-C. Shin, J.-S. Park and G.-P. Choi, *Sens. Actuators, B*, 2003, **96**, 717–722.

8 D. H. Yoon and G. M. Choi, *Sens. Actuators, B*, 1997, **45**, 251–257.

9 C. Liangyuan, L. Zhiyong, B. Shouli, Z. Kewei, L. Dianqing, C. Aifan and C. C. Liu, *Sens. Actuators, B*, 2010, **143**, 620–628.

10 P. Rai and Y.-T. Yu, *Sens. Actuators, B*, 2012, **161**, 748–754.

11 V. Galstyan, E. Comini, C. Baratto, G. Faglia and G. Sberveglieri, *Ceram. Int.*, 2015, **41**, 14239–14244.

12 L. Zhu and W. Zeng, *Sens. Actuators, A*, 2017, **267**, 242–261.

13 V. S. Bhati, M. Hojamberdiev and M. Kumar, *Energy Rep.*, 2020, **6**, 46–62.

14 M. Hjiri, L. El Mir, S. G. Leonardi, A. Pistone, L. Mavilia and G. Neri, *Sens. Actuators, B*, 2014, **196**, 413–420.

15 S. Bai, T. Guo, Y. Zhao, R. Luo, D. Li, A. Chen and C. C. Liu, *J. Mater. Chem. A*, 2013, **1**, 11335–11342.

16 N. L. Hadipour, A. Ahmadi Peyghan and H. Soleymanabadi, *J. Phys. Chem. C*, 2015, **119**, 6398–6404.

17 M. Maarouf and A. Al-Sunaidi, *Comput. Theor. Chem.*, 2020, **1175**, 112728.

18 C. Wöll, *Prog. Surf. Sci.*, 2007, **82**, 55–120.

19 U. Diebold, L. V. Koplitz and O. Dulub, *Appl. Surf. Sci.*, 2004, **237**, 336–342.

20 Q.-L. Tang and Q.-H. Luo, *J. Phys. Chem. C*, 2013, **117**, 22954–22966.

21 W. Kohn and L. J. Sham, *Phys. Rev.*, 1965, **140**, A1133–A1138.

22 G. Kresse and J. Hafner, *Phys. Rev. B: Condens. Matter Mater. Phys.*, 1993, **47**, 558–561.

23 G. Kresse and J. Hafner, *Phys. Rev. B: Condens. Matter Mater. Phys.*, 1994, **49**, 14251–14269.

24 G. Kresse and J. Furthmüller, *Phys. Rev. B: Condens. Matter Mater. Phys.*, 1996, **54**, 11169–11186.

25 G. Kresse and J. Furthmüller, *Comput. Mater. Sci.*, 1996, **6**, 15–50.

26 G. Kresse and D. Joubert, *Phys. Rev. B: Condens. Matter Mater. Phys.*, 1999, **59**, 1758–1775.

27 P. E. Blöchl, *Phys. Rev. B: Condens. Matter Mater. Phys.*, 1994, **50**, 17953–17979.

28 J. P. Perdew, J. A. Chevary, S. H. Vosko, K. A. Jackson, M. R. Pederson, D. J. Singh and C. Fiolhais, *Phys. Rev. B: Condens. Matter Mater. Phys.*, 1992, **46**, 6671–6687.

29 A. D. Becke, *Phys. Rev. A: At., Mol., Opt. Phys.*, 1988, **38**, 3098–3100.

30 J. P. Perdew, K. Burke and M. Ernzerhof, *Phys. Rev. Lett.*, 1996, **77**, 3865–3868.

31 H. J. Monkhorst and J. D. Pack, *Phys. Rev. B: Solid State*, 1976, **13**, 5188.

32 K. Harun, N. A. Salleh, B. Deghfel, M. K. Yaakob and A. A. Mohamad, *Results Phys.*, 2020, **16**, 102829.

33 X. Ma, Y. Wu, Y. Lv and Y. Zhu, *J. Phys. Chem. C*, 2013, **117**, 26029–26039.

34 W. Göpel, J. Pollmann, I. Ivanov and B. Reihl, *Phys. Rev. B: Condens. Matter Mater. Phys.*, 1982, **26**, 3144–3150.

35 T. L. M. Pham, S. Nachimuthu, J.-L. Kuo and J.-C. Jiang, *Appl. Catal., A*, 2017, **541**, 8–14.

36 T. L. M. Pham, D.-V. N. Vo, H. N. T. Nguyen and N.-N. Pham-Tran, *Appl. Surf. Sci.*, 2019, **481**, 1327–1334.

37 J. P. Prates Ramalho, F. Illas and J. R. B. Gomes, *Phys. Chem. Chem. Phys.*, 2017, **19**, 2487–2494.

38 S. Grimme, J. Antony, S. Ehrlich and H. Krieg, *J. Chem. Phys.*, 2010, **132**, 154104.

39 S. Grimme, S. Ehrlich and L. Goerigk, *J. Comput. Chem.*, 2011, **32**, 1456–1465.

40 C. B. Duke, A. R. Lubinsky, S. C. Chang, B. W. Lee and P. Mark, *Phys. Rev. B: Solid State*, 1977, **15**, 4865–4873.

41 C. B. Duke, R. J. Meyer, A. Paton and P. Mark, *Phys. Rev. B: Solid State*, 1978, **18**, 4225–4240.

42 D. J. Cooke, A. Marmier and S. C. Parker, *J. Phys. Chem. B*, 2006, **110**, 7985–7991.

43 N. R. D'Amico, G. Cantele and D. Ninno, *J. Phys. Chem. C*, 2012, **116**, 21391–21400.

44 B. Meyer and D. Marx, *Phys. Rev. B: Condens. Matter Mater. Phys.*, 2003, **67**, 035403.

45 M. J. S. Spencer, K. W. J. Wong and I. Yarovsky, *Mater. Chem. Phys.*, 2010, **119**, 505–514.

46 D. Ma, Z. Wang, H. Cui, J. Zeng, C. He and Z. Lu, *Sens. Actuators, B*, 2016, **224**, 372–380.

47 F. Maldonado, L. Villamagua and R. Rivera, *J. Phys. Chem. C*, 2019, **123**, 12296–12304.

48 R. G. S. Pala and H. Metiu, *J. Phys. Chem. C*, 2007, **111**, 8617–8622.

49 D. Ma, Q. Wang, T. Li, Z. Tang, G. Yang, C. He and Z. Lu, *J. Mater. Chem. C*, 2015, **3**, 9964–9972.

50 K. L. D'Amico, M. R. McClellan, M. J. Sayers, R. R. Gay, F. R. McFeely and E. I. Solomon, *J. Vac. Sci. Technol.*, 1980, **17**, 1080–1084.

51 R. R. Gay, M. H. Nodine, V. E. Henrich, H. J. Zeiger and E. I. Solomon, *J. Am. Chem. Soc.*, 1980, **102**, 6752–6761.

52 B. Meyer and D. Marx, *J. Phys.: Condens. Matter*, 2003, **15**, L89–L94.

53 Q. Yuan, Y.-P. Zhao, L. Li and T. Wang, *J. Phys. Chem. C*, 2009, **113**, 6107–6113.

54 M. Buchholz, X. Yu, C. Yang, S. Heißler, A. Nefedov, Y. Wang and C. Wöll, *Surf. Sci.*, 2016, **652**, 247–252.

55 C. Yang and C. Wöll, *Adv. Phys.: X*, 2017, **2**, 373–408.

56 P. Esser and W. Göpel, *Surf. Sci.*, 1980, **97**, 309–318.

57 M. Casarin, C. Maccato and A. Vittadini, *Appl. Surf. Sci.*, 1999, **142**, 192–195.

58 S. Tosoni, C. Li, P. Schlexer and G. Pacchioni, *J. Phys. Chem. C*, 2017, **121**, 27453–27461.

59 M. Andersen, X. Yu, M. Kick, Y. Wang, C. Wöll and K. Reuter, *J. Phys. Chem. C*, 2018, **122**, 4963–4971.

60 H. Shi, H. Yuan, S. Ruan, W. Wang, Z. Li, Z. Li and X. Shao, *J. Phys. Chem. C*, 2018, **122**, 8919–8924.

61 Y. Wang and C. Wöll, *Chem. Soc. Rev.*, 2017, **46**, 1875–1932.

62 C. Lamberti, A. Zecchina, E. Groppo and S. Bordiga, *Chem. Soc. Rev.*, 2010, **39**, 4951–5001.